

Ultra-high anisotropy and electronic property of two-dimensional $PbSnS_2$ with a black phosphorus structure

Xinlong Wang(王鑫龙), Shihao Wang(王诗皓), Yandi Jiang(姜彦迪), Qing Min(闵清), Haiming Huang(黄海铭), Chengrui Wu(吴承瑞), and Juntao Yang(杨俊涛)

Citation: Chin. Phys. B, 2026, 35 (**5**): 057304. DOI: 10.1088/1674-1056/ae1568
http://cpb.iphy.ac.cn; http://iopscience.iop.org/cpb

What follows is a list of articles you may be interested in

Exciton insulators in two-dimensional systems

Huaiyuan Yang(杨怀远), Xi Dai(戴希), and Xin-Zheng Li(李新征)
Chin. Phys. B, 2025, 34 (**9**): 097301. DOI: 10.1088/1674-1056/ade3ae

Moiré physics in two-dimensional materials: Novel quantum phases and electronic properties

Zi-Yi Tian(田子弈), Si-Yu Li(李思宇), Hai-Tao Zhou(周海涛), Yu-Hang Jiang(姜宇航), and Jin-Hai Mao(毛金海)
Chin. Phys. B, 2025, 34 (**2**): 027301. DOI: 10.1088/1674-1056/ad9e96

$GaInX_3$ (X = S, Se, Te): Ultra-low thermal conductivity and excellent thermoelectric performance

Zhi-Fu Duan(段志福), Chang-Hao Ding(丁长浩), Zhong-Ke Ding(丁中科), Wei-Hua Xiao(肖威华), Fang Xie(谢芳), Nan-Nan Luo(罗南南), Jiang Zeng(曾犟), Li-Ming Tang(唐黎明), and Ke-Qiu Chen(陈克求)
Chin. Phys. B, 2024, 33 (**8**): 087302. DOI: 10.1088/1674-1056/ad47e3

Effect of strain on structure and electronic properties of monolayer C_4N_4

Hao Chen(陈昊), Ying Xu(徐瑛), Jia-Shi Zhao(赵家石), and Dan Zhou(周丹)
Chin. Phys. B, 2024, 33 (**5**): 057302. DOI: 10.1088/1674-1056/ad260c

Anomalous valley Hall effect in two-dimensional valleytronic materials

Hongxin Chen(陈洪欣), Xiaobo Yuan(原晓波), and Junfeng Ren(任俊峰)
Chin. Phys. B, 2024, 33 (**4**): 047304. DOI: 10.1088/1674-1056/ad1c59

Ultra-high anisotropy and electronic property of two-dimensional $PbSnS_2$ with a black phosphorus structure

Xinlong Wang(王鑫龙), Shihao Wang(王诗皓), Yandi Jiang(姜彦迪), Qing Min(闵清), Haiming Huang(黄海铭), Chengrui Wu(吴承瑞)†, and Juntao Yang(杨俊涛)‡

Shiyan Key Laboratory of Quantum Information and Precision Optics, School of Optoelectronic Engineering, School of New Energy, Hubei University of Automotive Technology (HUAT), Shiyan 442000, *China*

(Received 1 August 2025; revised manuscript received 11 October 2025; accepted manuscript online 21 October 2025)

Novel two-dimensional materials with fascinating electronic structures hold promise for applications in electronics, optoelectronics, and sensor devices. In this work, the mechanical, anisotropic，and electronic properties of $PbSnS_2$ monolayer, which adopts a black-phosphorus-like structure, were systematically investigated using density functional theory calculations. The $PbSnS_2$ monolayer is identified as an indirect band gap semiconductor. The band gap is predicated to be 1.22 eV and 1.69 eV by PBE functional and HSE06 methods, respectively. Notably, it exhibits a high anisotropic carrier mobility as $\mu_e = 4.46 \times 10^3$ $cm^2 \cdot V^{-1} \cdot s^{-1}$ with electrons preferentially transporting along the zigzag direction. The band gap can be effectively narrowed under the strains in the armchair direction whereas enlarged in the zigzag direction. In addition, $PbSnS_2$ monolayer exhibits strong optical absorption in visible-light and ultra-visible regions. Our findings suggest that the ultra-high anisotropy in both carrier mobility and optical absorption makes $PbSnS_2$ monolayer a promising candidate for applications in unipolar field-effect transistors and photosensitive devices. This study provides valuable insights for future exploration of low-dimensional materials with tailored functionalities.

Keywords: two-dimensional materials, electronic structures, anisotropic properties, first-principles calculations

PACS: 71.20.–b, 73.63.–b, 78.20.–e, 71.15.Mb

DOI: 10.1088/1674-1056/ae1568 **CSTR:** 32038.14.CPB.ae1568

1. Introduction

Two-dimensional (2D) materials are emerging as very promising candidates for fabricating high performance semiconductor devices, owing to their high carrier mobility, excellent optoelectronic performance and tunable electronic structure. As is well known, the carrier mobility of graphene-based field-effect transistors can be up to 1.5×10^4 $cm^2 \cdot V^{-1} \cdot s^{-1}$,[1,2] while transition metal sulfides (TMDs) with an excellent photocatalytic activity in visible region have been successfully incorporated into photodetectors.[3,4] The family of layered transition metal phosphorous trichalcogenides with tunable band gaps has been proposed as a novel candidate for field-effect transistors and ultraviolet region photodetectors.[5,6] In particular, black phosphorus (BP) has garnered a substantial attention due to its unique puckered structure and intrinsic anisotropic behavior.[7] BP monolayer displays a direct band gap of 1.70 eV and an intrinsic carrier mobility up to 1×10^5 $cm^2 \cdot V^{-1} \cdot s^{-1}$ along its zigzag direction,[8] highlighting its potential for next-generation electronic technologies.[9] However, the high chemical reactivity of BP, particularly its susceptibility to oxidation and hydrolysis in ambient conditions, poses significant challenges for its integration into high-performance electronic devices.[10,11] As a consequence, extensive efforts have focused on exploring more puckered-structure (named as BP-structured) materials, including single-element, binary and ternary elements. These BP-structured materials include polymeric nitrogen,[12,13] black arsenic,[14] and binary IV–VI compounds (e.g., SnS and SnSe),[15,16] which has expanded the library of 2D BP-structured candidates for high-performance electronic devices. Notably, ternary IV–VI compounds offer additional degrees of freedom in tailoring physical properties through compositional engineering., including solar cells,[17] radiation detectors,[18] optical switching devices,[19] and spin transport devices,[20] etc. Recently, BP-structured $PbSnS_2$ monolayer can be expected to exhibit pronounced anisotropic properties due to its ternary-element composition, making them a compelling target for fundamental and applied research.[21–23]

In usual, $PbSnS_2$ crystal exhibits two distinct phases: an NaCl-type rock salt structure and an orthorhombic mineral phase known as teallite.[24,25] The cubic $PbSnS_2$ was predicated to be a narrow band gap semiconductor (about 0.2 eV), which is thermodynamically unstable in the bulk state but can be stabilized in the form of nanoparticles.[24] Teallite is a naturally layered semiconductor with a direct band gap about 1.6 eV, it can act as an n-type high-performance thermoelectric material by effective Cl or Ni doping.[26,27] In the teallite

†Corresponding author. E-mail: crwu@huat.edu.cn

‡Corresponding author. E-mail: jtyang@huat.edu.cn

© 2026 Chinese Physical Society and IOP Publishing Ltd. All rights, including for text and data mining, AI training, and similar technologies, are reserved.

crystal structure, Pb and Sn atoms form a layered sheet covalently bonded with S atoms, with adjacent layers held together by van de Waals (vdW) forces. Ultrathin $PbSnS_2$ flakes have been synthesized successfully by chemical vapor deposition from teallite crystal, demonstrating giant anisotropy in charge carrier mobility and optoelectronic responsivity.[22] In addition, $PbSnS_2$ flakes can be obtained by mechanical exfoliation method, exhibiting a strong angular and temperature dependence in Raman scattering intensity.[21] Interestingly, a density functional theory (DFT) study show that the band gap shows an indirect-to-direct transition by compressive stress in armchair direction, while by tensile stress in zigzag direction.[23] These findings suggest that 2D $PbSnS_2$ monolayer can possess an ultra-high anisotropic character in optical absorption,[22] thermal transport,[26] and electronic properties,[23] respectively.

Up to now, despite the observation of pronounced in-plane anisotropy in $PbSnS_2$ monolayers, their anisotropic mechanical properties and electronic structures remain incompletely explored. In this work, the mechanical, electronic, and optical properties of $PbSnS_2$ were systematically studied by means of first-principles calculations based on DFT. Our results predict that 2D $PbSnS_2$ is an indirect band gap semiconductor with a robust dynamics and mechanical stability. Owing to its ultra-high in-plane anisotropy, strain engineering can modulate the band gap anisotropically: uniaxial strain enlarges the band gap along the armchair direction while reducing it along the zigzag direction. Furthermore, the band structure exhibits multi-peak dispersion near the band edges and shows an electron mobility as high as 4.46×10^3 $cm^2 \cdot V^{-1} \cdot s^{-1}$ along the zigzag direction with significantly lower values observed in other crystallographic directions.

2. Methods

First-principles calculations were performed by the Vienna *Ab initio* Simulation Package (VASP) within the projector-augmented-wave (PAW) method.[30,31] Exchange and correlation interactions were treated by the generalized gradient approximation (GGA) using Perdew–Burke–Ernzerhof (PBE) functional,[32] additionally, the Heyd–Scuseria–Ernzerhof (HSE06) hybrid functional[33,34] was employed to obtain a more accurate band gap value. Wave functions were expanded in a plane-wave basis set with a kinetic energy cut-off of 500 eV. Convergence criterion were set to 1×10^{-8} eV for total energy and 1×10^{-3} eV/Å for atomic forces, respectively. The 2D Brillouin zone was sampled using a $16 \times 16 \times 1$ k-mesh within the Monkhorst–Pack scheme for electronic structure calculations with the tetrahedron method by Blöchl corrections.[32,35] A 15-Å vacuum was adopted to avoid the interactions between two adjacent periodic layers. DFT-D3 method was used for vdW force correction in all calculations.[36] *Ab initio* molecular dynamics (AIMD) simulations were performed by Nosé–Hoover thermostat method.[37,38] Phonon spectra were calculated via the finite displacement method using PHONOPY code.[39] To avoid the artifacts from vacuum layer thickness, optical absorption spectra of 2D sheets were calculated from the optical conductivity within the independent-quasiparticle approximation of the complex dielectric function.[40,41] Data visualization was performed by VESTA program[42] and the VASPKIT package[43] were employed for data processing.

3. Results and discussion

3.1. Crystal structure and stability of $PbSnS_2$ monolayer

As illustrated in Fig. 1(a), the fully relaxed structure of $PbSnS_2$ monolayer belongs to *Pnma* space group symmetry and contains four atoms (Pb, Sn, S_1, and S_2) in its unit cell.[28,41] From a top view, $PbSnS_2$ monolayer forms a continuous network of rectangular-like lattices, showing a difference with the hexagonal honeycomb structure of BP monolayer. Similar to the significant in-plane anisotropy of BP, $PbSnS_2$ monolayer displays two distinct in-plane directions:[44] one along the $\boldsymbol{a}$ vector (zigzag direction), where the atomic chains exhibit periodic undulations forming a wavy and corrugated structure, and the other one along the $\boldsymbol{b}$ vector (armchair direction), where atomic chains are arranged in parallel. From the side view, $PbSnS_2$ monolayer consists of two sublayers, with Sn atoms in the upper sublayer and Pb atoms in the lower sublayer. Each S atom covalently bonds to one Pb and one Sn atom, contributing to the corrugated structure along the armchair direction. These optimized lattice parameters, including lattice constants, bond lengths and bond angles, were listed in Table 1. Notably, the lattice constant $a = 4.10$ Å is shorter than $b = 4.40$ Å, showing an excellent consistency with the experimental values,[28,29] such as $a = 4.06$ Å and $b = 4.28$ Å[29] respectively. The calculated monolayer thickness $c = 2.73$ Å is approximately twice 1.20 Å of BP.[45] This non-planar geometry shows more rigid bond angles and shorter bond lengths in armchair direction than the corresponding parameters in zigzag direction, respectively. For example, the bond Sn–S_1 has a length of 2.69 Å which is shorter than 2.73 Å of Sn–S_2, while the angle $\angle S_1$–Pb–S_2 is 80.86° and smaller than 90.78° of $\angle S_1$–Sn–S_2. Since the angle values of $\angle S_1$–Pb–S_2 and $\angle S_1$–Sn–S_2 are near 90°, Sn and Pb atoms appear nearly aligned above S atoms from the top view, leading to the rectangular-like lattice morphology. This crystal geometry underpins the unique mechanical and electronic anisotropy of $PbSnS_2$ monolayer.

Cleavage energy E_{cl} is a measurement of the energy required to split a bulk material into two separate layers, herein, E_{cl} can be used to evaluate the feasibility of obtaining a $PbSnS_2$ monolayer by mechanical exfoliation methods.

The cleavage energy was calculated using the formula $E_{\rm cl} = (2E_{\rm 2D} - E_{\rm bulk})/A$, where A is the area of unit cell, $E_{\rm 2D}$ is the energy of a single monolayer and $E_{\rm bulk}$ represents the energy of a bulk crystal constructed from two monolayers. The calculated cleavage energy of $PbSnS_2$ is $E_{\rm cl} = 0.49$ J/m^2, which is in good agreement with previous result of 0.51 J/m^2.[23] This cleavage energy is higher than ~ 0.38 J/m^2 of BP[46] and ~ 0.36 J/m^2 of graphene[47] whereas lower than 0.91 J/m^2 of 2D GeP_3[48] and 1.09 J/m^2 of 2D Ga_2N,[49] respectively, indicating that $PbSnS_2$ monolayer can be fabricated via mechanical exfoliation from its bulk crystal.[21] AIMD simulations were performed at 300 K, the time-dependent energy fluctuations and AIMD-relaxed structure were presented in Fig. 1(b). Obviously, the energy fluctuates smoothly over 10 ps, in addition, both the top and side snapshots of the relaxed monolayer confirm structural integrity with no bond breakage, demonstrating high thermal stability. As presented in Fig. 1(c), the phonon spectra composed of 3 acoustic branches and 12 optical branches, exhibiting positive phonon frequencies throughout most of the Brillouin zone except for minor negative frequencies near the Γ point, which can be attributed to numerical inaccuracies in inter-atomic force calculations with a small supercell.[50] Therefore, the $PbSnS_2$ monolayer is considered dynamically stable. Herein, $PbSnS_2$ monolayer can be considered as a dynamically stable structure. The elastic moduli of 2D $PbSnS_2$ were studied from energy-strain method by $C_{ij} = \partial^2 E_{\rm ela}/(A^2 \partial\delta_x \partial\delta_y)$, where $E_{\rm ela}$ is the total energy and δ_x is the external stress applied via $\delta = \Delta a/a$.[43,51] A series of strains were applied from -5% to 5% with a step 1%. There are five independent elastic constants were obtained: $C_{11} = 59.06$ N/m, $C_{22} = 51.48$ N/m, $C_{12} = C_{21} = 35.38$ N/m and $C_{66} = 33.90$ N/m. These elastic constants well satisfy the Born criteria of $C_{11}C_{22} - C_{12}^2 > 0$ and $C_{66} > 0$, confirming an excellent mechanical stability of $PbSnS_2$ monolayer.[52]

In addition, the orientation-dependent Young's modulus $Y(\theta)$, shear modulus $G(\theta)$ and Poisson's ratio $\nu(\theta)$ were calculated to characterize the mechanical anisotropy of $PbSnS_2$ monolayer,[53,54] as plotted in Figs. 2(a), 2(b), and 2(c), respectively. Notably, Young's modulus along the $\boldsymbol{a}+\boldsymbol{b}$ or $\boldsymbol{a}-\boldsymbol{b}$ direction is significantly higher than along the zigzag or armchair direction. For instance, $Y(\theta)$ increases steadily from a minimum of 30.28 N/m in the armchair direction to a maximum of 77.68 N/m near $\theta = 45°$. Additionally, the maximum Young's modulus in the armchair direction is lower than that in the zigzag direction. As a consequence, $PbSnS_2$ monolayer shows a pronounced mechanical anisotropy: it undergoes significant deformation under tensile stress along the $\boldsymbol{a}$ or $\boldsymbol{b}$ axis, whereas shear stress applied along the $\boldsymbol{a}+\boldsymbol{b}$ or $\boldsymbol{a}-\boldsymbol{b}$ directions more readily induces deformation. The value of 77.68 N/m is far lower than $Y = 341.60$ N/m of graphene, thus, $PbSnS_2$ monolayer is more susceptible to in-plane strain engineering. Interestingly, Poisson's ratios are 0.5 in the zigzag direction and 0.7 in the armchair direction, respectively, denoting abnormal lateral expansion under tension and contraction under compression.

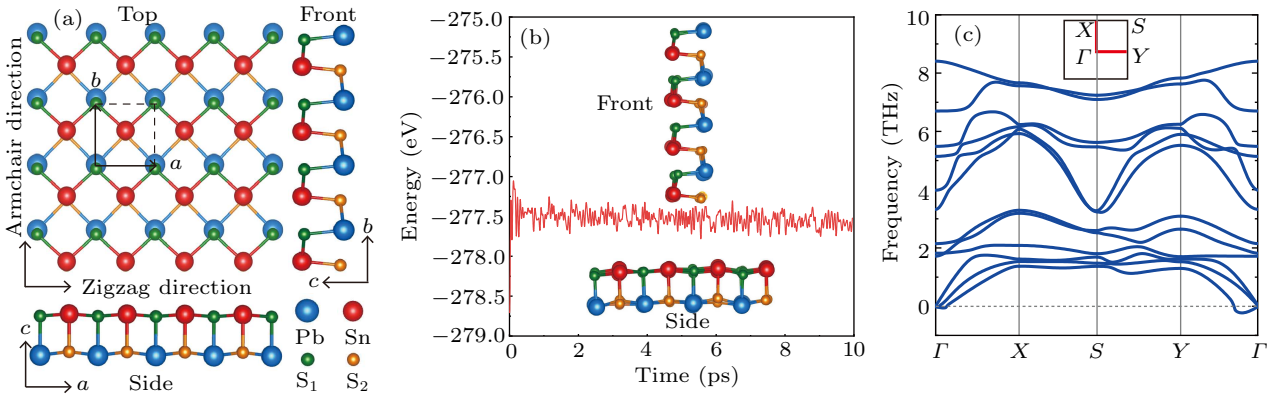


Fig. 1. For 2D $PbSnS_2$, (a) crystal structure in top, front, and side views, its unit cell is indicated by the lattice vectors with broken lines; (b) energy fluctuations during AIMD simulations at 300 K, the snapshots indicate front and side views of relaxed monolayer; (c) phonon dispersion, Brillouin zone is inserted with high-symmetry points.

Table 1. Present (Pres.) calculated lattice constant with the monolayer thickness c^* (in unit Å), bond length (in unit Å), and bond angle (°) of 2D $PbSnS_2$, comparing to some experiment (Expt.) and theory (Theo.) results.

Object	Lattice constant			Bond length				Bond angle	
Parameter	a	b	c^*	Sn–S_1	Sn–S_2	Pb–S_1	Pb–S_2	∠S_1–Sn–S_2	∠S_1–Pb–S_2
Pres.	4.10	4.40	2.73	2.69	2.73	3.08	2.59	80.86	90.78
Expt.	3.99[28]	4.20							
	4.06[29]	4.28							
Theo.	4.32[23]	4.15	2.89	2.61	2.74	3.18	2.67	79.90	89.65
	4.06[29]	4.22							

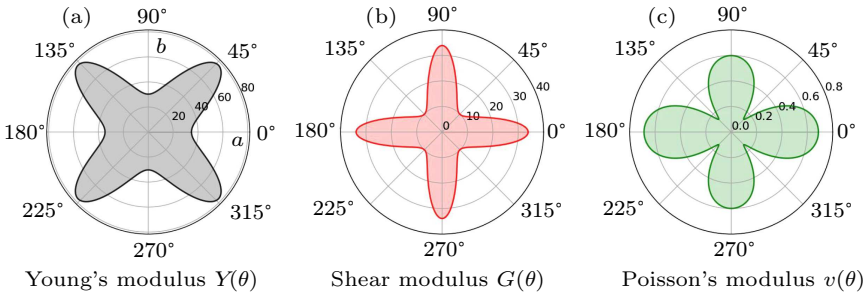


Fig. 2. Orientation-dependent (a) Young's modulus, (b) shear modulus and (c) Possion's ratio as a function of the in-plane angle θ for 2D $PbSnS_2$, 0° is along the zigzag direction.

3.2. Electronic structure of $PbSnS_2$ monolayer

In usual, the anisotropy is not only a geometrical effect but also manifests in electronic structures.[55] Here, the band structures calculated using the PBE functional were plotted in Fig. 3(a). Clearly, $PbSnS_2$ monolayer is an indirect band gap semiconductor with the valence band (VB) maximum (VBM) near the Y point and the conduction band (CB) minimum (CBM) near X point, respectively. The calculated band gap of 1.22 eV is larger than experimental case of 0.99 eV[26] or calculated value of 1.08 eV[56] for the bulk state, as a result of the well-known quantum confinement effect. Neither the CBM nor the VBM is located at Γ point as the center of Brillouin zone, but the CB exhibits positive parabolic dispersion and the VB displays negative features, consistent with typical behavior. Notably, the top VB has a pronounced energy minimum and the bottom CB has a distinct maximum near the S point as a corner of Brillouin zone. Interestingly, a unique double-peak features appear at the band edges near the X and Y points as the side of reduced Brillouin zone: two maxima peaks appear in top VB near the X point with the VBM located at X–Γ high-symmetry line. Correspondingly, two minima valleys appear in bottom CB with the CBM located in the X–S high-symmetry line, demonstrating the significant anisotropy of electronic structure. To directly examine the anisotropy of band dispersion, the three-dimensional (3D) versions of bottom CB and top VB with their 2D projections in the Brillouin zone were shown in Figs. 4(a) and 4(b), respectively. The high-symmetry lines of Γ–X and Γ–Y were technologically expanded to twice its length in order to have a clear view on 3D versions. Similar to the crystal structure, the band structures also exhibit a C_2 symmetry on the 3D version. The most striking character is a very towering peak for bottom CB and very deep valley for top VB near S point. Notably, the multi-peak features can be clearly observed for the bottom CB and top VB near the X and Y high-symmetry points, which will play an vital role in the carrier mobility and optical property of $PbSnS_2$ monolayer.

Since the GGA method usually underestimates semiconductor band gaps, the HSE06 hybrid functional was employed to obtain more accurate band structures, also plotted in Fig. 3(a). As expected, the HSE06 calculated band gap of 1.69 eV is much larger than 1.22 eV obtained by PBE functional. Our PBE band gap 1.22 eV is a little smaller than previous results about 1.50 eV,[22,23] while our HSE06 value 1.69 eV is larger than these theory values. Although there are some difference between calculated band gaps, the VBM and CBM positions remain at the same k points for PBE method and HSE06 hybrid functional. Besides that the HSE06 CBs shift up about 0.47 eV compared with PBE bands, the HSE06 bands show similar dispersion compared with those of PBE bands, particularly for the top VB. Therefore, the PBE results were focused on in subsequent discussions for simplicity.

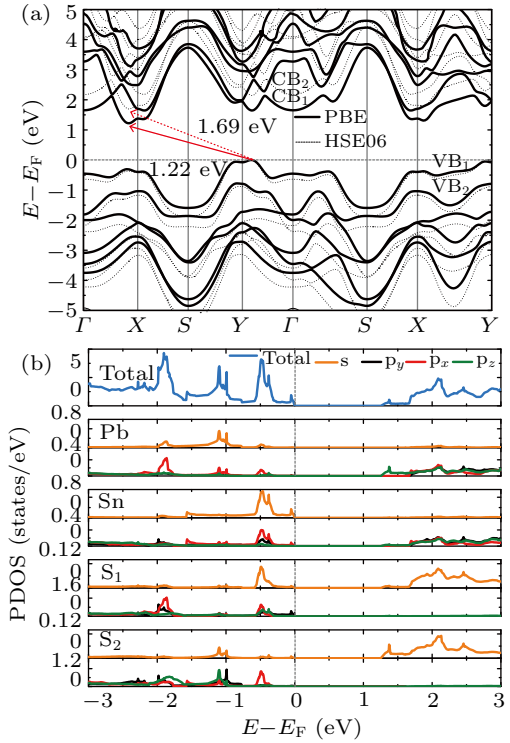


Fig. 3. (a) Band structures of 2D $PbSnS_2$ calculated by PBE and HSE06 levels, respectively, the band gap is indicated by red arrow. (b) Total DOS and orbital-projected DOS of each atom for 2D $PbSnS_2$.

In order to clarify the detailed compositions of band structures, the total density of states (DOS) and orbital-projected DOS (PDOS) of each atom were illustrated in Fig. 3, while the orbital-weighted band structures of each atom were depicted in Fig. 5, respectively. Notably, the orbital-weighted band structures display that the occupied states of VBs are

mostly contributed by sulfur electrons whereas the unoccupied states of CBs are mainly dominated by metal electrons. Electronic states near the CBM are mostly contributed by significant hybridization between Pb p_x and S_2 s orbitals, evident in the partial charge density of the CBM, as illustrated in Fig. 4(c). Meanwhile, electronic states near the VBM are mainly composed of strong hybridization between Sn s and S_1 p_y orbitals, as directly visualized by the partial charge density of VBM, as illustrated in Fig. 4(d). This high anisotropy of electronic states observed near the band edges aligns with the crystal structure anisotropy, for instance, the bond length of Pb–S_2 (2.59 Å) is significantly shorter than 3.08 Å of Pb–S_1, as listed in Table 1. Besides the CBM and VBM, two distinct energy regions exhibit electron concentration due to strong orbital hybridization. One energy region is around −0.5 eV where the electronic states are mostly dominated by Sn and S_1 orbitals. The second energy region near −1.0 eV is concentrated with Pb and S_2 electrons. Orbital hybridization between sulfur and metal orbitals is further confirmed by the orbital-weighted band structures, as illustrated in Figs. 5(a)–5(d), respectively. Owing to the strong hybridization between S orbitals and Pb/Sn orbitals, $PbSnS_2$ monolayer exhibits the excellent mechanical stability and properties.

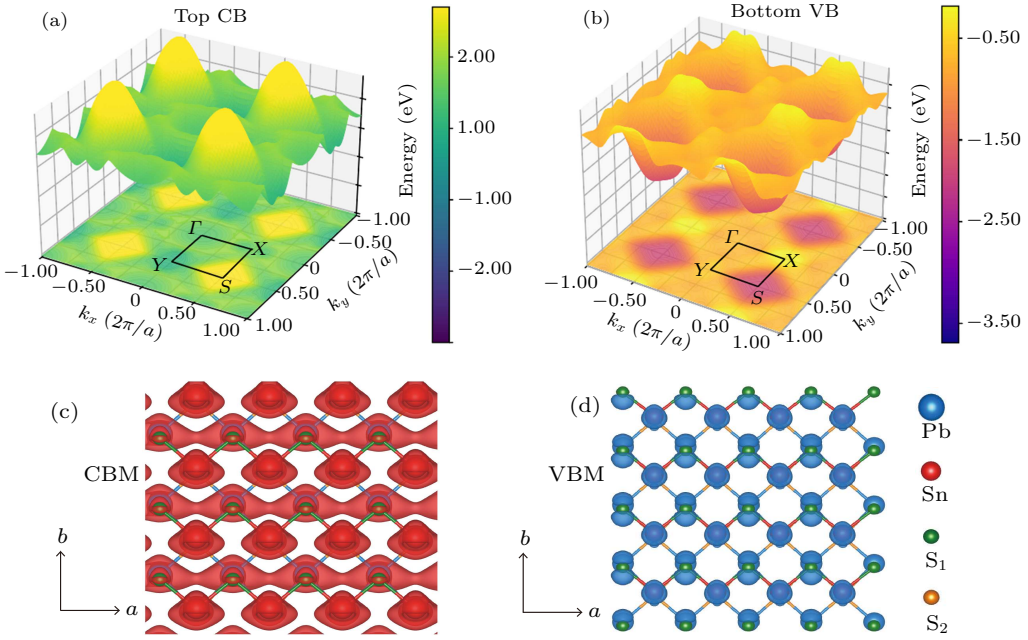


Fig. 4. For 2D $PbSnS_2$, 3D versions of panel (a) top CB and panel (b) bottom VB along with their projections in Brillouin zone (here the sides of Brillouin zone were technologically translated to twice its length), partial charge density maps of panel (c) CBM and panel (d) VBM with an isosurface of 0.1×10^{-3} $e/\text{Å}^3$.

3.3. Carrier mobility of $PbSnS_2$ monolayer

Since the carrier mobility μ strongly depends on band edges, now the electron mobility μ_e and hole mobility μ_e were investigated to evaluate the anisotropic transport properties of $PbSnS_2$ monolayer. Based on deformation potential (DP) theory, the carrier mobility of 2D materials can be described by the following expression:[57–61]

$$\mu_{2D} = \frac{e\hbar^3 C_{2D}}{k_B T m^* m_d E_d^2}, \tag{1}$$

where the parameters T, e, $\hbar$, and k_B indicates the temperature set to be 300 K, electron charge, reduced Planck constant, and Boltzmann constant, respectively. m_d is the average effective mass defined as $m_d = \sqrt{m_x^* m_y^*}$, where m_x^* is the effective mass along a specific direction x. E_d is the deformation potential which indicates the shift of the band edge induced by stress $\delta = \Delta a/a$, read as

$$E_d = \Delta E_{edge}/\delta, \tag{2}$$

where ΔE_{edge} is the energy difference of CBM/VBM before and after applying stress. As listed in Table 2, the in-plane stiffness $C_{2D} = 61.47$ N/m along the zigzag direction is larger than 52.20 N/m along the armchair direction, this feature is consistent with the mechanical properties discussed above. Notably, the most remarkable mobility is $\mu_e = 4.46 \times 10^3$ $\text{cm}^2\cdot\text{V}^{-1}\cdot\text{s}^{-1}$ in the zigzag direction, in well agreement with the previous theory value of $\mu_e = 2.70 \times 10^3$ $\text{cm}^2\cdot\text{V}^{-1}\cdot\text{s}^{-1}$.[23] This highest electron mobility is about four times larger than the $\mu_e = 1.14 \times 10^3$ $\text{cm}^2\cdot\text{V}^{-1}\cdot\text{s}^{-1}$ of black phosphorus[8] and approximately 20 times higher than the $\mu_e = 7.20 \times 10$ $\text{cm}^2\cdot\text{V}^{-1}\cdot\text{s}^{-1}$ of MoS_2.[62] This highest electron mobility $\mu_e = 4.46 \times 10^3$ $\text{cm}^2\cdot\text{V}^{-1}\cdot\text{s}^{-1}$ aligns with the smallest DP constant $|E_d| = 0.77$ eV along with the smallest effective masses of $0.64m_0$. Correspondingly, the lowest mobility $\mu_h = 6.32$ $\text{cm}^2\cdot\text{V}^{-1}\cdot\text{s}^{-1}$ in the zigzag direction corresponds to the largest effective mass of $1.83m_0$ combined with a large DP constant $|E_d| = 9.50$ eV. Correspondingly, the small

carrier mobility in the armchair direction is also attributed to its large DP constant. This anisotropic carrier mobility is directly visualized in the partial charge density maps, as illustrated in Fig. 4(c) of CBM and Fig. 4(d) of VBM, respectively. The VBM exhibits no electron overlap, resulting in poor carrier transport channels in the armchair direction, whereas the CBM shows significant overlap, particularly along the zigzag direction, providing an excellent pathway for electron transport. That is to say, $PbSnS_2$ monolayer has a high electron transport in zigzag direction but a low hole mobility.[23] Such mobility anisotropy highlights the potential of $PbSnS_2$ monolayer as an outstanding material for fabricating unipolar diodes in high-speed switching devices. Additionally, anisotropic carrier mobility facilitates electron–hole separation with minimal recombination, rendering the monolayer advantageous for optoelectronic applications.[63]

Table 2. In-plane stiffness C_{2D} (in units N/m), absolute DP constant $|E_d|$ (in unit eV), absolute effective mass m^* and a average effective mass m_d (m_0, the distinct mass of a free electron), carrier mobility μ (in units $cm^2 \cdot V^{-1} \cdot s^{-1}$) for electron e and hole h of VBM and CBM along the zigzag and armchair directions for 2D $PbSnS_2$, respectively.

Direction	Carrier	C_{2D}	$\|E_d\|$	m^*	m_d^*	μ
Zigzag	e	61.47	0.77	0.64	0.78	4.46×10^3
	h		9.50	1.84	1.25	6.32
Armchair	e	52.20	10.03	0.81	1.19	11.50
	h		6.55	0.94	1.11	25.00

Owing to the electronic structures of BP monolayer can be efficiently tuned by uniaxial strains,[64,65] the band structures of BP-structured $PbSnS_2$ monolayer were explored in further by applying uniaxial stress ranging from -5% to $+5\%$ with a step 1%. Compared to the pristine band structures near the Fermi level, selected band structures under different strains in the zigzag and armchair directions were plotted in Figs. 6(a) and 6(b), respectively. Under uniaxial tension (compression), both the CBs and VBs shift towards higher (lower) energy levels across the entire Brillouin zone, except for a narrow range along the high-symmetry Y–Γ line. This trend is consistent for both zigzag and armchair directions relative to the pristine state. Interestingly, the most significant deformation occurs at the X point under uniaxial strains in the zigzag direction, especially for the CBs. This results in the smallest DP energy of 0.77 eV, which is advantageous for the high electron mobility (μ_e) as discussed above.

The energy varies under the uniaxial strains in the zigzag and armchair directions for VBM and CBM were presented in Fig. 6(c), respectively. Notably, in the zigzag direction, the VBM energy remains nearly constant, while the CBM energy decreases with increasing uniaxial strains, leading to a widening of the band gap. The uniaxial strain dependence of the band gaps was illustrated in Fig. 6(d). In the armchair direction, both the VBM and CBM energies decrease with strain, however, the VBM energy decreases more slowly than the CBM energy, resulting in a narrowing of the band gap. When the applied compressive strain reaches -5%, the band gap of $PbSnS_2$ becomes 0.7 eV in the zigzag direction and 1.46 eV in the armchair direction. At a tensile strain of $+5\%$, the band gap increases to 1.6 eV in the zigzag direction and decreases to 1.18 eV in the armchair direction. As expected, the band gap can be efficiently and anisotropically tuned by uniaxial strains, which makes a promise for $PbSnS_2$ applications in sensor devices.

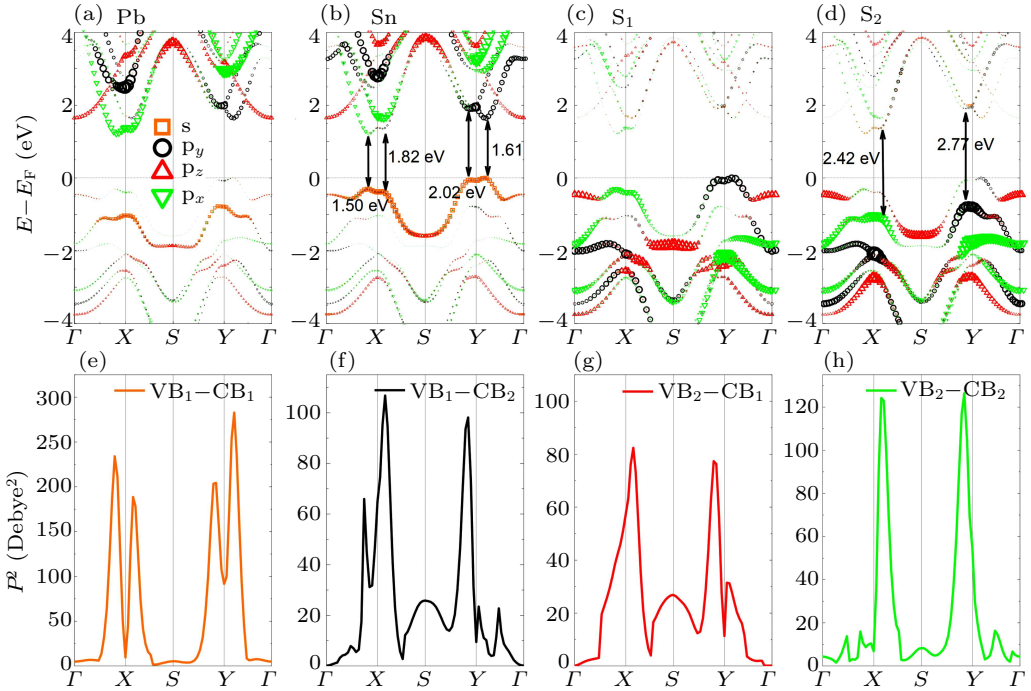


Fig. 5. Orbital-weighted band structures of atom (a) Pb, (b) Sn, (c) S_1, and (d) S_2, respectively. Transition dipole moment in square form as P^2 of electronic transitions between (e) VB_1 and CB_1, (f) VB_1 and CB_2, (g) VB_2 and CB_1, (h) VB_2 and CB_2, respectively.

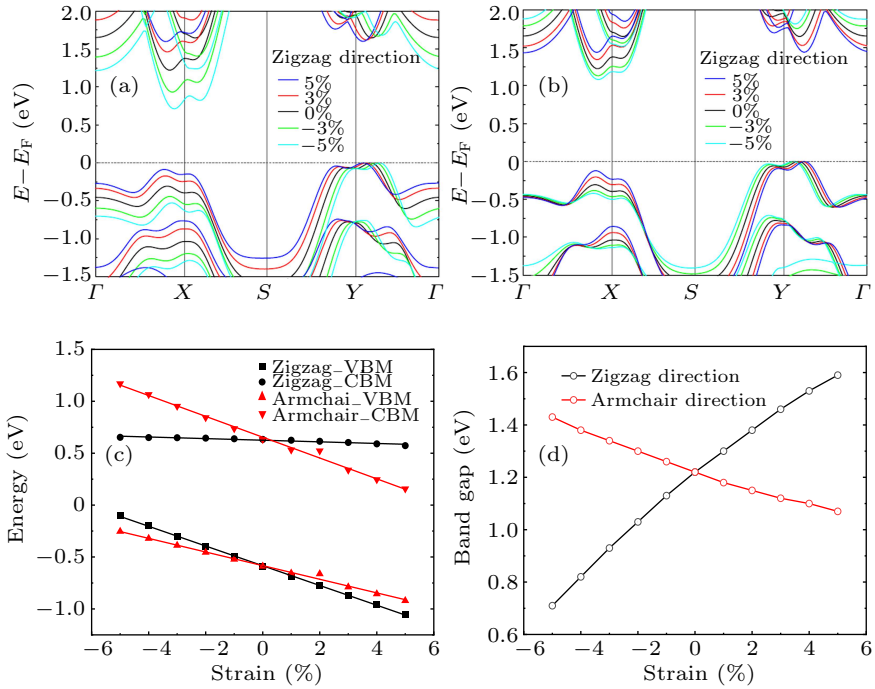


Fig. 6. For 2D $PbSnS_2$, band dispersion near the Fermi level under uniaxial strains in (a) zigzag and (b) armchair directions, respectively. (c) Energy varies under uniaxial strain in the zigzag and armchair directions of the CBM and VBM, respectively. (d) Band gaps of $PbSnS_2$ as a function of uniaxial strain in the zigzag and armchair directions, respectively.

3.4. Optical property of $PbSnS_2$ monolayer

Owing to the unique dispersion of multi-peak band edges near the high-symmetry points, $PbSnS_2$ monolayer is expected to exhibit excellent optical absorption. The absorbance of 2D $PbSnS_2$ calculated using the PBE method in the zigzag (xx) direction and armchair direction (yy) was plotted in Fig. 7, respectively. Due to the indirect band gap, the absorbance curve increases slowly when the photon energy exceeds the band gap of 1.22 eV. The first absorption peak in the zigzag direction occurs at 1.66 eV with an absorbance of 2.5%, which is half the value of the first absorption peak of 5.0% at 1.82 eV in the armchair direction. Subsequently, the second absorption peak appears around 2.40 eV with an absorbance about 12% in the zigzag direction and near 11% in the armchair direction. Besides the absorption peaks in the visible range, the absorbance continues to increase, reaching the strongest and broadest absorption peaks in the ultraviolet range. These peaks have an absorbance exceeding 15% in the zigzag direction and near 20% in the armchair direction. As a consequence, $PbSnS_2$ monolayer shows a strong optical absorption in the visible and ultraviolet range, which is in accordance to the experimental observation.[29]

Based on the entire symmetry and spatial overlap of electronic wave functions, the transition dipole moment (TDM) P between initial and final electronic states was calculated to investigate the origin of visible-region absorption peaks in $PbSnS_2$ monolayer.[66,67] Typically, the square of TDM magnitude as P^2 represents the transition probability between two states.[41] The variations of P^2 along the high-symmetry line were plotted in Figs. 5(e)–5(h) to illustrate the transition probabilities between the initial VBs of VB_1 VB_2 and final CBs of CB_1, CB_2, respectively. Here, VB_1 and VB_2 indicates the top and second top VB while CB_1 and CB_2 indicates the bottom and second bottom CB, respectively, as labeled in Fig. 3(a). Clearly, the electronic transitions are predominantly allowed near X and Y high-symmetry points, whereas the transitions are nearly forbidden at Γ point and exhibit very low probability at S point. As can be seen, the absorbance peak near 1.66 eV originates from the electronic transitions between S_1 p_y and Sn s states of VB_1 to Pb p_y and Sn p_y states of CB_1 near the Y point, the peak at 1.82 eV is from the transitions between Sn s states of VB_1 to Pb p_x states of CB_1 near X point, the peaks around 2.40 eV are mostly from the transitions between S_2 p_x states of VB_2 to Pb p_y states of CB_1 near X point. These TDM results demonstrate that S, Pb and Sn all play crucial roles in the optical properties of $PbSnS_2$ monolayer.

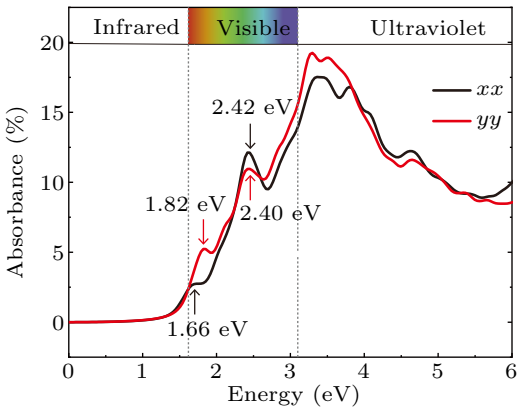


Fig. 7. Optical absorbance of 2D $PbSnS_2$ calculated by PBE functional. The arrows indicate the energies of absorption peaks.

4. Conclusion

In this study, the mechanical, electronic and optical properties of 2D $PbSnS_2$ monolayers were thoroughly investigated using first-principles calculations based on DFT. The BP-structured $PbSnS_2$ monolayer displays excellent dynamical stability, as confirmed by phonon spectra calculations, and mechanical stability, as evidenced by the satisfaction of the Born criteria for the elastic constants. The mechanical properties exhibit significant anisotropy, with the Young's modulus and shear modulus showing directional dependence. $PbSnS_2$ is identified as a semiconductor with an indirect band gap of 1.22 eV, which can be anisotropically tuned by applying uniaxial strains. The calculated carrier mobility shows a pronounced anisotropy, with electron mobility reaching $\mu_e = 4.46 \times 10^3$ $cm^2 \cdot V^{-1} \cdot s^{-1}$ along the zigzag direction. The optical absorption characteristics of $PbSnS_2$ monolayer exhibit two distinct peaks in the visible range for both zigzag and armchair directions besides the strongest absorbance in the ultraviolet range. The transition dipole moment analysis indicates that the electronic transitions near the X and Y points are primarily responsible for these absorption peaks. Our findings reveal that $PbSnS_2$ monolayer exhibits remarkable anisotropy and unique electronic and optical characteristics, making it a promising candidate for high-speed switching devices, advanced sensor devices and excellent optoelectronic applications.

Acknowledgements

Project supported by the Natural Science Foundation of Hubei Province, China (Grant No. 2023AFB456), the Fund for Innovation Team in Colleges for Science and Technology of Hubei Province, China (Grant No. T2021012), the Doctoral Scientific Research Foundation of HUAT (Grant Nos. BK202483, BK202302, and BK202208), the Fund for Hubei Key Laboratory of Energy Storage and Power Battery (Grant No. QCCLSZK2021A06), and the Open Foundation Project of Hubei Key Laboratory of Optical Information and Pattern Recognition (Grant No. 202403) of Wuhan Institute of Technology and College Students Innovation and Entrepreneurship Training Program (Grant Nos. DC2023074 and DC2024087) of HUAT.

References

[1] Geim A K 2009 *Science* **324** 1530
[2] Novoselov K S, Geim A K, Morozov S V, Jiang D E, Zhang Y, Dubonos S V, Grigorieva I V and Firsov A A 2004 *Science* **306** 666
[3] Falkovsky L A 2008 *J. Phys.: Conf. Ser.* **129** 012004
[4] Kang D H, Kim M S, Shim J, Jeon J, Park H Y, Jung W S, Yu H Y, Pang C H, Lee S and Park J H 2015 *Adv. Funct. Mater.* **25** 4219
[5] Liu J, Li X B, Wang D, Lau W M, Peng P and Liu L M 2014 *J. Chem. Phys.* **140** 054707
[6] Yang J T, Xu C J, Wang H J, Min Q, Luo S J, Xiong Y C, Ren W and Jing C 2023 *J. Phys.: Conden. Matter* **35** 395501
[7] Li L, Yu Y, Ye G J, Ge Q, Ou X, Wu H, Feng D, Chen X H and Zhang Y 2014 *Nat. Nanotechnol.* **9** 372
[8] Qiao J, Kong X, Hu Z X, Yang F and Ji W 2014 *Nat. Commun.* **5** 4475
[9] Li L, Kim J, Jin C, Ye G J, Qiu D Y, Da Jornada F H, Shi Z, Chen L, Zhang Z, Yang F, *et al*. 2017 *Nat. Nanotechnol.* **12** 21
[10] Woomer A H, Farnsworth T W, Hu J, Wells R A, Donley C L and Warren S C 2015 *ACS Nano* **9** 8869
[11] Brent J R, Savjani N, Lewis E A, Haigh S J, Lewis D J and O'Brien P 2014 *Chem. Commun.* **50** 13338
[12] Laniel D, Winkler B, Fedotenko T, Pakhomova A, Chariton S, Milman V, Prakapenka V, Dubrovinsky L and Dubrovinskaia N 2020 *Phys. Rev. Lett.* **124** 216001
[13] Ji C, Adeleke A A, Yang L, Wan B, Gou H, Yao Y, Li B, Meng Y, Smith J S, Prakapenka V B, *et al.* 2020 *Sci. Adv.* **6** eaba9206
[14] Chen Y, Chen C, Kealhofer R, Liu H, Yuan Z, Jiang L, Suh J, Park J, Ko C, Choe H S, *et al*. 2018 *Adv. Mater.* **30** 1800754
[15] Makinistian L and Albanesi E 2006 *Phys. Rev. B* **74** 045206
[16] Baumgardner W J, Choi J J, Lim Y F and Hanrath T 2010 *J. Am. Chem. Soc.* **132** 9519
[17] Xu X, Song Q, Wang H, Li P, Zhang K, Wang Y, Yuan K, Yang Z, Ye Y and Dai L 2017 *ACS Applied Materials & Interfaces* **9** 12601
[18] Pejova B and Tanuševski A 2008 *J. Phys. Chem. C* **112** 3525
[19] Zhang C, Ouyang H, Miao R, Sui Y, Hao H, Tang Y, You J, Zheng X, Xu Z, Cheng X, *et al*. 2019 *Adv. Opt. Mater.* **7** 1900631
[20] Shi G and Kioupakis E 2015 *Nano Lett.* **15** 6926
[21] Łapińska A, Taube A, Wąsik M, Żukowska G Z, Duzynska A, Judek J and Zdrojek M 2017 *Journal of Raman Spectroscopy* **48** 479
[22] Shu Z, Peng Q, Huang P, Xu Z, Suleiman A A, Zhang X, Bai X, Zhou X and Zhai T 2020 *Matter* **2** 977
[23] Xu W, Xie Z, Su J, Wang R, Wu X and Xu H 2021 *J. Phys. Chem. Lett.* **12** 10574
[24] Soriano R, Malliakas C, Wu J and Kanatzidis M 2012 *J. Am. Chem. Soc.* **134** 3228
[25] Frisenda R, Niu Y, Gant P, Muñoz M and Castellanos-Gomez A 2020 *npj 2D Materials and Applications* **4** 38
[26] Zhan S, Hong T, Qin B, Zhu Y, Feng X, Su L, Shi H, Liang H, Zhang Q, Gao X, *et al*. 2022 *Nat. Commun.* **13** 5937
[27] Zhan S, Bai S, Qin B, Zhu Y, Wang S, Liu D, Hong T, Gao X, Zheng L, Wen Y, *et al*. 2024 *Adv. Funct. Mater.* **34** 2406428
[28] Girard S N, Chasapis T C, He J, Zhou X, Hatzikraniotis E, Uher C, Paraskevopoulos K M, Dravid V P and Kanatzidis M G 2012 *Energy & Environmental Science* **5** 8716
[29] Acharyya P, Pal K, Zhang B, Barbier T, Prestipino C, Boullay P, Raveau B, Lemoine P, Malaman B, Shen X, *et al*. 2024 *J. Am. Chem. Soc.* **146** 13477
[30] Kresse G and Furthmüller J 1996 *Phys. Rev. B* **54** 11169
[31] Perdew J P, Burke K and Ernzerhof M 1996 *Phys. Rev. Lett.* **77** 3865
[32] Monkhorst H J and Pack J D 1976 *Phys. Rev. B* **13** 5188
[33] Kümmel S and Kronik L 2008 *Rev. Mod. Phys.* **80** 3
[34] Heyd J, Scuseria G E and Ernzerhof M 2003 *J. Chem. Phys.* **118** 8207
[35] Blöchl P E, Jepsen O and Andersen O 1994 *Phys. Rev. B* **49** 16223
[36] Marom N, Tkatchenko A, Rossi M, Gobre V V, Hod O, Scheffler M and Kronik L 2011 *Journal of Chemical Theory and Computation* **7** 3944
[37] Barnett R N and Landman U 1993 *Phys. Rev. B* **48** 2081
[38] Braga C and Travis K P 2005 *J. Chem. Phys.* **123** 134101
[39] Togo A, Oba F and Tanaka I 2008 *Phys. Rev. B* **78** 134106
[40] Matthes L, Pulci O and Bechstedt F 2014 *New J. Phys.* **16** 105007
[41] Wang V, Tang G, Liu Y C, Wang R T, Mizuseki H, Kawazoe Y, Nara J and Geng W T 2022 *J. Phys. Chem. Lett.* **13** 11581
[42] Momma K and Izumi F 2011 *Journal of Applied Crystallography* **44** 1272
[43] Wang V, Xu N, Liu J C, Tang G and Geng W T 2021 *Comput. Phys. Commun.* **267** 108033
[44] Jiang J W and Park H S 2014 *J. Phys. D: Appl. Phys.* **47** 385304
[45] Xia F, Wang H and Jia Y 2014 *Nat. Commun.* **5** 4458
[46] Shulenburger L, Baczewski A, Zhu Z, Guan J and Tomanek D 2015 *Nano Lett.* **15** 8170
[47] Jin Y, Li X and Yang J 2015 *Phys. Chem. Chem. Phys.* **17** 18665
[48] Jing Y, Ma Y, Li Y and Heine T 2017 *Nano Lett.* **17** 1833
[49] Zhao S, Li Z and Yang J 2014 *J. Am. Chem. Soc.* **136** 13313
[50] Cahangirov S, Topsakal M, Aktürk E, Sahin H and Ciraci S 2009 *Phys. Rev. Lett.* **102** 236804

[51] Cadelano E, Palla P L, Giordano S and Colombo L 2010 *Phys. Rev. B* **82** 235414

[52] Mouhat F and Coudert F X 2014 *Phys. Rev. B* **90** 224104

[53] Gao Z D, Jiang Z H Y, Li J D, Li B W, Long Y Y, Li X M, Yin J and Guo W L 2022 *Adv. Eng. Mater.* **24** 2200519

[54] Wang V, Tang G, Liu Y, Wang R T, Mizuseki H, Kawazoe Y, Nara J and Geng W 2022 *J. Phys. Chem. Lett.* **13** 11581

[55] Yin Y, Shao C, Zhang C, Zhang Z, Zhang X, Robertson J and Guo Y 2020 *ACS Applied Materials & Interfaces* **12** 22378

[56] Chen Z, Ming H, Li Z, Girard S N, Morris C D, Guo W, Wu M, Yu Y, Wolverton C, Luo Z Z, *et al.* 2025 *Angewandte Chemie* **137** e202501667

[57] Bardeen J and Shockley W 1950 *Phys. Rev.* **80** 72

[58] Bruzzone S and Fiori G 2011 *Appl. Phys. Lett.* **99** 222108

[59] Chen J, Xi J, Wang D and Shuai Z 2013 *J. Phys. Chem. Lett.* **4** 1443

[60] Dai J and Zeng X C 2015 *Angewandte Chemie International Edition* **54** 7572

[61] Zhang S, Xie M, Li F, Yan Z, Li Y, Kan E, Liu W, Chen Z and Zeng H 2016 *Angewandte Chemie* **128** 1698

[62] Rawat A, Jena N, De Sarkar A, *et al*. 2018 *J. Mater. Chem. A* **6** 8693

[63] Zhang X, Zhao X, Wu D, Jing Y and Zhou Z 2016 *Adv. Sci.* **3** 1600062

[64] Lin Z, Tian Z, Cen W and Zeng Q 2023 *Physica B* **657** 414780

[65] Deng Y, Zhang Y, Zhao Y, Xu Y, Dai X, Wang S, Lu X, Li Y, Xu Y and He L 2024 *Chin. Phys. Lett.* **41** 037102

[66] Wang H J, Yang J T, Xu C J, Huang H M, Min Q, Xiong Y C and Luo S J 2022 *J. Phys.: Condens. Matter* **35** 014002

[67] Wang G, Du Y N, Huang P, Qian Z F, Zhang P and Wei S H 2025 *Phys. Rev. Lett.* **134** 036401